JOURNAL OF
SYNCHROTRON
RADIATION

ISSN 1600-5775

The coherent radiation fraction of low-emittance synchrotrons

Harry Westfahl Jr,* Sérgio A. Lordano Luiz, Bernd C. Meyer and Florian Meneau

Brazilian Synchrotron Light Laboratory – LNLS, CNPEM, CP 6192, 13083-970 Campinas, SP, Brazil.
*Correspondence e-mail: westfahl@lnls.br

Received 5 October 2016
Accepted 23 February 2017

Edited by J. F. van der Veen

Keywords: coherence; Gaussian–Schell; diffraction-limit storage ring.

In this work the coherence properties of the synchrotron radiation beam from an X-ray undulator in a fourth-generation storage ring are analyzed. A slightly focused X-ray beam is simulated using a wavefront propagation through a non-redundant array of slits and the mutual coherence function is directly obtained and compared with the Gaussian–Schell approximation. The numerical wave propagation and the approximate analytical approaches are shown to agree qualitatively, and it is also shown that, when the coherent fraction is selected by a finite aperture before the focusing element, even achromatic focusing systems like total reflection mirrors become slightly chromatic. This effect is also well accounted for in the Gaussian–Schell model. The wavefront propagation simulation through the non-redundant array was repeated with an imperfect mirror demonstrating that, although the wavefront is distorted, its coherent length is practically unchanged.

1. Introduction

Coherence is the manifestation of purity of a quantum state of light or matter (Mandel & Wolf, 1965). The concept of coherence has long been associated with interference, simply because it is the most direct way of measuring it. In the case of the electromagnetic radiation produced by electron beams in storage rings, although a single electron emits a fully coherent beam, the photons produced by the multiple electrons in a storage ring add up incoherently (Kim, 1985). The radiation observed is then the result of a classical mixture of the photon states emitted by many electrons, randomly distributed over a finite region of the electron beam phase-space, whose volume is the so-called emittance (Bazarov, 2012). Consequently, the smaller the emittance, the purer is the quantum state of the radiation and the higher the degree of coherence.

A simple qualitative way of stating the pureness (loosely called coherent fraction) of the radiation emitted by an electron beam in a storage ring is to compare its natural emittance (r.m.s. source divergence × r.m.s. source size) with the limiting emittance of the electromagnetic radiation, determined by the Heisenberg uncertainty principle. In a Gaussian radiation beam the latter is given (in practical units) by $\varepsilon_{\rm r}$ [pm rad] = $\lambda/4\pi \simeq 100/\hbar\omega$ [keV]. This qualitative boundary is also commonly referred to as the diffraction limit. Consequently, since the electrons in third-generation storage rings have natural emittances of the order of 1 nm rad, they reach the diffraction limit in the soft X-ray energy range (photon energies of the order of $\hbar\omega \simeq 0.1$ keV). In fourth-generation storage rings, like Sirius and MAX IV, on the other hand, the horizontal emittances are of the order of 100 pm rad and, therefore, the diffraction limit is reached in the tender X-rays

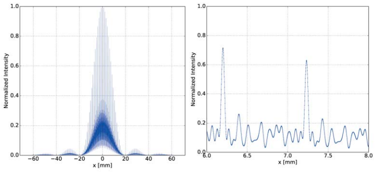

energy range (photon energies of the order of $\hbar\omega \simeq 1$ keV). This diffraction limit criterion, based only on the emittance, is nevertheless incomplete and quantitatively misleading. Although the photons emitted by a single electron in an undulator are fully coherent, their phase space is not well described by a Gaussian distribution and the actual photon emittance is about twice as large, closer to $\lambda/2\pi$. In other words, even the radiation emitted by an undulator in a (theoretical) zero emittance storage ring would not achieve the $\lambda/4\pi$ limit.

The classical mixture imposed by the electrons is expressed through a convolution of the phase-space distribution of the photons in pure states (Wigner distribution function) and the phase-space distribution of the electrons (Kim, 1985; Bazarov, 2012; Tanaka, 2014). Such convolution is not solely dependent upon the volume of the phase-space of the electron beam ($\varepsilon_{\rm e} = \sigma_{\rm e}\sigma_{\rm e}'$) but also on its aspect ratio, the so-called beta function ($\beta_{\rm e} = \sigma_{\rm e}/\sigma_{\rm e}'$). For a fixed emittance, it has been proved (Lindberg & Kim, 2015) that this convolution is minimized (and the purity of the state is maximized) when the electron beam beta function is approximately equal to the radiation beta function, given by $\beta_{\rm r} = L_{\rm u}/\pi$, where $L_{\rm u}$ is the undulator length. Thus, only when this last condition is met can one (still qualitatively) state that for energies of the order of $\hbar\omega$ [keV] < $100/\varepsilon_{\rm e}$ [pm rad] the emittance of the electron beam is near the diffraction limit. For instance, comparing the two latest fourth-generation synchrotrons, Sirius and MAX IV, both have emittances of about 200 pm rad. However, since in the Sirius storage ring $\beta_{\rm e} \simeq 1.5$ m (horizontal direction), a 3–4 m X-ray undulator is close to the optimal condition ($\beta_{\rm e} \simeq \beta_{\rm r}$) while in MAX IV $\beta_{\rm e} \simeq 9$ m, and thus $\beta_{\rm e} \gg \beta_{\rm r}$. Therefore, theoretically, it is expected that the effective radiation emittance will be almost two times smaller in Sirius than in MAX IV.

In this paper the coherence properties of a slightly focused X-ray beam emitted from an X-ray undulator in the Sirius storage ring is analyzed, simulating a wavefront propagation (Chubar *et al.*, 2011, 2013) through a non-redundant array (NRA) of slits. This strategy was explored experimentally by Skopintsev *et al.* (2014) and here it was used to directly extract the mutual coherence function. The results from these simulations are then compared with the Gaussian–Schell approximation for the propagation of the X-ray beam, assuming the r.m.s. size and divergence of the synchrotron radiation beam from an X-ray undulator are described by the universal function proposed by Tanaka & Kitamura (2009).

2. Estimating coherence

Coherence is exploited in most scientific programs of third- and fourth-generation synchrotrons in coherent diffraction imaging techniques, X-ray photon correlation spectroscopy and nano-focusing (Veen & Pfeiffer, 2004). One of the main goals in designing beamlines for these experiments is to preserve the coherent wavefront and to maximize the amount of coherent flux reaching the sample. In order to quantify coherence one needs to determine how much correlation exists between the electric field in different points of the illuminated area. This is done through the normalized mutual coherence function (or complex degree of coherence) defined as (Mandel & Wolf, 1965)

$$\gamma(\mathbf{r},\mathbf{r}';\tau) = \frac{\langle E^*(\mathbf{r},t)\,E(\mathbf{r}',t+\tau)\rangle}{[I(\mathbf{r})]^{1/2}[I(\mathbf{r}')]^{1/2}},$$

where $\mathbf{r} = (x,y)$ is the transverse coordinate vector, $I(\mathbf{r}) = \langle E(\mathbf{r},t)^2\rangle$ is the time average beam intensity, and $E(\mathbf{r},t)$ and $E(\mathbf{r}',t+\tau)$ are the field values at the positions $\mathbf{r}$ and $\mathbf{r}'$ and times t and $t+\tau$. The brackets $\langle\ldots\rangle$ denote the time or ensemble average, assuming stationary and ergodic wavefields. In the context of interference experiments the function γ appears as the contrast of the interference fringes. Note that $1 > |\gamma(\mathbf{r},\mathbf{r}';\tau)| > 0$, spanning the limits between full coherence and complete incoherence.

Even in fourth-generation storage rings the coherence is limited in the X-ray energy range. The use of apertures to select the coherent portion of the radiation phase-space is paramount. However, as these apertures become comparable with the transverse coherence length of the beam, diffraction effects can change the focusing properties of the optical elements in a way that is substantially different from the intuitive geometric optics. A detailed analysis of the transverse coherence properties of the synchrotron radiation, based on statistical optics and Fourier optics, was presented by Geloni *et al.* (2008). In this work it has been shown that, in the diffraction limit, the propagation properties of the undulator radiation deviate substantially from those of a partially coherent Gaussian beam. Indeed, in all simulations performed here, such behavior in the vertical direction was observed. Nonetheless, as will be shown, the so-called Gaussian–Schell model for a partially coherent Gaussian beam qualitatively captures many important aspects of the wavefront propagation in the horizontal direction, which in fourth-generation storage rings is near the diffraction limit for tender X-rays. This separation between the two transverse directions of propagation is allowed in the paraxial approximation, normally valid for synchrotron radiation beam propagation. Therefore, in this work the coherence properties analysis is restricted to the horizontal direction.

In the Gaussian–Schell model (Friberg & Turunen, 1988; Dragoman, 1995; Vartanyants & Singer, 2010; Schroer & Falkenberg, 2014; Singer & Vartanyants, 2014) the irradiance distribution and the degree of coherence are both Gaussian and described by the following expressions,

$$I(\mathbf{r},z=0) \propto \exp\left(-\frac{x^2}{2\sigma_x^2}\right)\exp\left(-\frac{y^2}{2\sigma_y^2}\right), \qquad (1)$$

$$\gamma(\mathbf{r}-\mathbf{r}',z=0) \propto \exp\left[-\frac{(x-x')^2}{2\xi_x^2}\right]\exp\left[-\frac{(y-y')^2}{2\xi_y^2}\right]. \qquad (2)$$

Here, $\sigma_{x(y)}$ is the r.m.s. dimensions of the beam and $\xi_{x(y)}$ is the transverse coherence length, in both the horizontal (vertical) direction. The correlation length in the Gaussian–Schell model is a simple function of the r.m.s. beam size σ and the coherent fraction ζ (for each direction), expressed as

$$\xi = \frac{2\sigma}{\left(\zeta^{-2} - 1\right)^{1/2}}. \tag{3}$$

One interesting aspect of this model is that the coherent fraction, ζ, is simply determined by the ratio of the limiting emittance and the actual radiation emittance,

$$\zeta = \frac{\lambda}{4\pi\sigma\sigma'}, \tag{4}$$

where σ' is the r.m.s. beam divergence.

Note, however, that this model is an oversimplification of the radiation emitted by an undulator. Even for a single electron radiation of an undulator, the emittance is $\sigma\sigma' \simeq \lambda/2\pi$, and this simplified analysis would lead to a coherent fraction of at most $\zeta \simeq 0.5$. Nevertheless, some qualitative aspects of the wavefront propagation can still be investigated using the Gaussian–Schell model, provided the r.m.s. size and divergence of the undulator radiation are chosen appropriately, as explained next.

3. Gaussian approximation to the undulator radiation

The exact description of the propagation of synchrotron radiation is challenging since the most common situation is partial coherence and neither geometrical optics (complete incoherence) nor Fresnel propagation (complete coherence) apply (Geloni *et al.*, 2008). A number of computer codes have already been developed for numerical characterization of synchrotron radiation taking into account partial coherence effects. The most comprehensive code, *SRW* (Chubar *et al.*, 2011, 2013), now allows a complete characterization taking into account all finite emittance effects. However, this kind of computation with a few thousand macro-electrons (Chubar *et al.*, 2011, 2013) can take several hours, even using multi-core computing systems. On the other hand, most approximated analytical approaches start from a Gaussian description of the photon phase space for treating its propagation. With these approaches, however, there are several different ways of defining the size and divergence of the undulator radiation, which depend on how the undulator radiation field is fitted to a Gaussian function (Lindberg & Kim, 2015).

A relatively simple analytical formula that allows a good approximation was proposed by Tanaka & Kitamura (2009). This approach for the r.m.s. size and divergence of the radiation from an undulator takes into account simultaneously the finite emittance and the energy spread of the electron beam in the storage ring. In fact, for higher harmonics the latter can be comparable with or even larger than the finite emittance effect. In this approximation, for each transverse direction the r.m.s. size and divergence of the beam are given by

$$\sigma \approx \left[\varepsilon\beta + \frac{\lambda L_{\rm u}}{2\pi^2}\,\mathcal{N}\left(\delta_\gamma/4\delta_n\right)^{2/3}\right]^{1/2}, \tag{5}$$

$$\sigma' \approx \left[(\varepsilon/\beta) + \frac{\lambda}{2L_{\rm u}}\,\mathcal{N}\left(\delta_\gamma/\delta_n\right)\right]^{1/2}, \tag{6}$$

where ε is the transverse electron beam emittance, β is the value of the beta function in the center of the undulator, $L_{\rm u}$ is the undulator length and $\mathcal{N}$ is a normalization factor that comes directly from the energy spread of the electron beam,

$$\mathcal{N}(\nu) = \frac{8\pi^2\nu^2}{(2\pi)^{3/2}\nu\,\mathrm{erf}\left[\left(8\pi^2\right)^{1/2}\nu\right] + \exp\left(-8\pi^2\nu^2\right) - 1},$$

with $\nu = \delta_\gamma/\delta_n$ being the ratio between the electron beam energy spread $\delta_\gamma = O(0.1\%)$ and the relative bandwidth $\delta_n = 1/nN_{\rm u}$ of the nth harmonic of single electron radiation from an undulator with $N_{\rm u}$ periods. Equations (5) and (6) describe qualitatively the effects of finite energy spread, more relevant in higher harmonics. Accounting for this effect is especially important for the storage rings of 3 GeV or less because higher harmonics are frequently used for harder X-rays.

Therefore, for analyzing qualitatively the wave propagation simulations, the Gaussian–Schell model is adopted [equations (1) to (4)], using parameters described by equations (5) and (6). The source of radiation is in the center of a 2 m 19 mm-period undulator in the low-beta straight section ($\beta_x \simeq \beta_y \simeq$ 1.5 m) of the Sirius storage ring (Liu *et al.*, 2014), with emittances ε_x = 245 pm rad and ε_y = 2.4 pm rad (bare machine). The beam size and divergence obtained from the universal function in this situation are shown in Fig. 1.

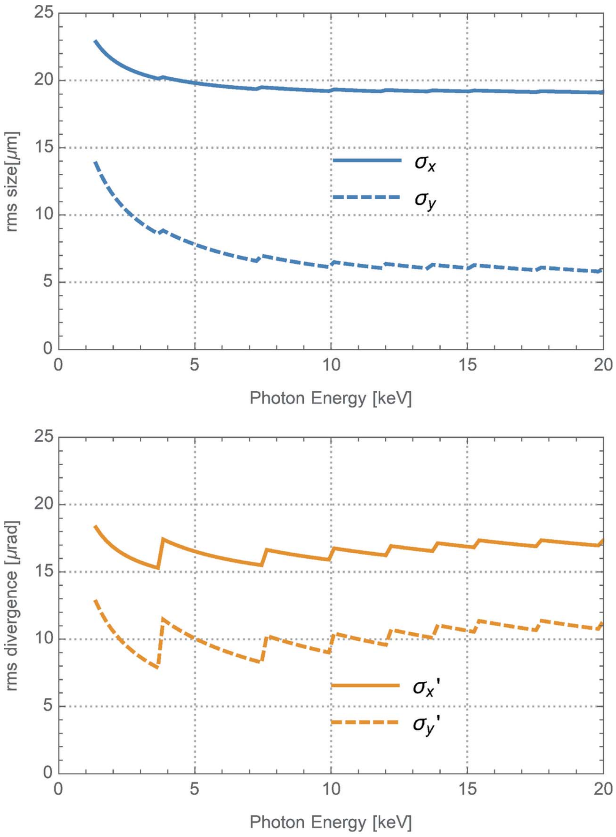

Figure 1
RMS source size and divergence of the 2 m U19 undulator in the Sirius storage ring according to the universal functions from equations (5) and (6) proposed by Tanaka & Kitamura (2009).

Table 1
Positions of the beamline elements used in the wavefront propagation (VFM = vertical focusing mirror, HFM = horizontal focusing mirror).

	Position (p)	Focal length (f)	Geometric focal point (q)
VFM	27 m	17.9 m	80 m
HFM	45 m	19.7 m	80 m

4. Optical layout for the simulations

In the simulations the synchrotron radiation beam is slightly focused to produce a micrometer-sized illuminated area at the focal position where the NRA diffraction grating lies. This situation is ideal for simulating single-shot diffractive imaging of micrometer-sized objects (Miao *et al.*, 2015). Although the analysis is mostly concerned with the horizontal direction of the beam, the beamline layout in the simulations includes a vertical focusing mirror (VFM) such that an approximately circular focal spot is formed at the NRA position (80 m from the source). The VFM produces approximately 1:2 focusing in the vertical direction, and the horizontal focusing mirror (HFM) produces approximately 1:1 focusing in the horizontal direction with optical elements according to Table 1 and Fig. 2. This results in an illumination spot at the focal position of approximately 20 µm × 20 µm (r.m.s.). Since in the horizontal direction the beam is only partially coherent, an aperture is positioned immediately before the HFM (Fig. 2) to select only the coherent fraction of the beam, effectively reducing its divergence acceptance. Another option would be to reduce the effective source size by creating a secondary source through a primary focusing optics and placing an aperture at the secondary focal point. Here the first approach is employed to reduce the number of optical elements and simplify the numerical simulations.

To analyze the coherence properties of the X-ray beam in the horizontal direction, the r.m.s. size and divergence are assumed as in Fig. 1 together with the analytical expressions for the propagation of a Gaussian–Schell beam through the beamline sketched in Fig. 2. The beam propagates through a set of thin optical elements (aperture and focusing mirror), with a total transfer matrix given by the product of their individual *ABCD* transfer matrices (Dragoman, 1995; Kauderer, 1991), as described in Appendix *A*.

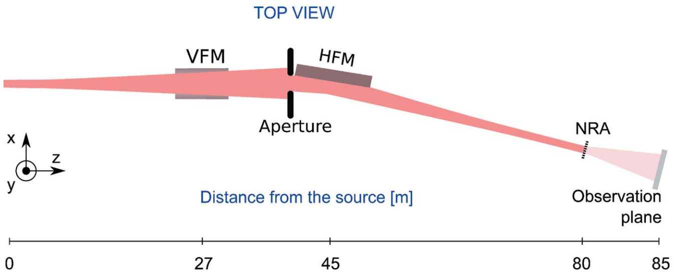

Figure 2
Schematics of the beamline layout used in the simulations of the NRA diffraction pattern.

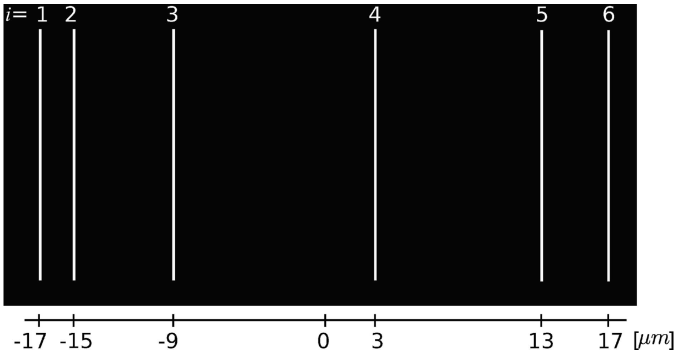

Figure 3
Schematics of the NRA of slits used in the wavefront propagation simulations.

5. Coherence length from numerical simulations

The mutual coherence function can be directly extracted from simulated diffraction patterns of double slits, at different slit separations, to determine the coherence length. Here, instead of running a double-slit experiment for each slit separation, a single diffraction simulation is performed using NRA. The important property of the NRA is that any pair formed between two different slits of the pattern (such as the ones shown in Fig. 3) will have a separation distance never replicated by any second pair. Conversely, all possible slit separations correspond to a single pair of slits (or none eventually), as listed in Table 2. This non-redundancy allows the diffraction patterns of many slit pairs to be isolated, simultaneously, in a single simulation or experiment. Such a strategy was explored experimentally by Skopintsev *et al.* (2014) and here was also proven very suitable for simulating coherence properties with *SRW*.[1] This approach gives the mutual coherence function in a single simulation, typically requiring about 14 h with 26 cores (Xeon E5440 at 2.83 GHz) for about 10000 macro-electrons.

The NRA is defined by a grating with 0.1 µm × 1 mm vertical slits, positioned in a Golomb ruler (Skopintsev *et al.*, 2014) with slits positions at $x_1 = -17$ µm, $x_2 = -15$ µm, $x_3 = -9$ µm, $x_4 = 3$ µm, $x_5 = 13$ µm and $x_6 = 17$ µm (Fig. 3), with $x = 0$ being the beam center. These positions were chosen to optimize the illuminated area and the diffraction patterns. The wavefront propagation is calculated for both transverse directions with *SRW* for the optical layout presented in Fig. 2 up to the plane where the diffraction pattern is observed at 5 m from the NRA. The beam intensity distribution is finally integrated in the vertical direction to obtain the one-dimensional diffraction pattern, like the one shown in Fig. 4, which is analyzed through the Gaussian–Schell model.

All distances between pairs of slits appearing in the diffraction pattern are presented in Table 2. Note that a single diffraction simulation of this NRA is equivalent to 15 simulations of pairs of slits, separated by distances ranging between 2 µm and 34 µm, at every 2 µm. The only distances which

---

[1] *SRW* also allows for calculating, in one partially coherent simulation, the 'mutual coherence' as a function of two horizontal or two vertical conjugate coordinates in the horizontal or in the vertical plane.

Table 2
Distances corresponding to each pair of slits in the diffraction pattern.

i, j	1, 2	5, 6	2, 3	1, 3	4, 5	3, 4	4, 6	2, 4	1, 4	3, 5	3, 6	2, 5	1, 5	2, 6	1, 6
x_{ij} (µm)	2	4	6	8	10	12	14	18	20	22	26	28	30	32	34

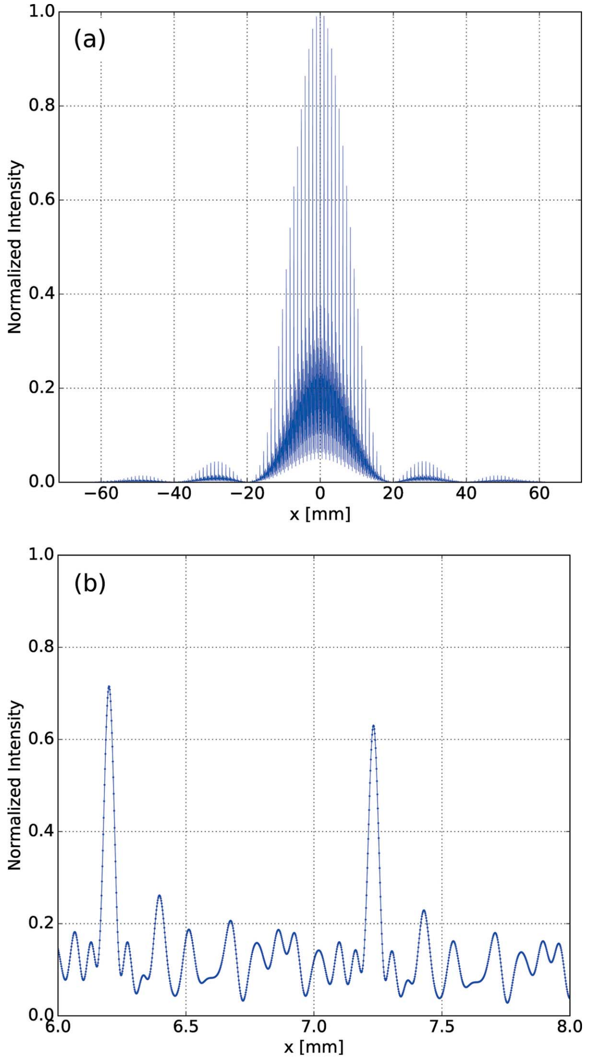

Figure 4
(*a*) *SRW* simulation of the interference pattern produced by the NRA obtained by vertical integration of the full diffraction pattern. (*b*) Zoom in the diffraction pattern from (*a*) to highlight the density of points calculated in the diffraction pattern.

cannot be formed using this Golomb ruler (and consequently do not appear in the diffraction pattern) are 16 µm and 24 µm.

As shown by Skopintsev *et al.* (2014), the far-field diffraction pattern, $I(\mathbf{q})$, of this grating is given by

$$I(q_x) = I_{\rm slit}(q_x)\left[C_0 + 2\sum_{i>j}^{N} \gamma_{ij}\left(I_i I_j\right)^{1/2}\cos\left(q_x x_{ij}\right)\right], \qquad (7)$$

where $C_0 \equiv \sum_i^N I(x_i)$, $\gamma_{ij} = \gamma(x_i - x_j)$ and $I_i \equiv I(x_i)$.

Once the diffraction pattern from equation (7) is Fourier transformed it yields

$$\tilde{I}(\delta x) \propto C_0 \tilde{T}_{\rm slit}(\delta x) + 2\sum_{i>j}^{N} \gamma_{ij}\left(I_i I_j\right)^{1/2} \tilde{T}_{\rm slit}\left(\delta x - x_{ij}\right),$$

where $\tilde{T}_{\rm slit}$ is a triangular function resultant from the convolution of the slit transmission and the delta function of the diffraction peaks. Therefore, the Fourier transform of the diffraction pattern from the NRA of slits is a set of triangular peaks, centered at the possible values of $x_i - x_j$, whose intensity is modulated by the mutual coherence function, $\Gamma(x_i, x_j) = \gamma(x_i - x_j)[I(x_i)\, I(x_j)]^{1/2}$. In the Gaussian–Schell model this is written as

$$\Gamma(x_i, x_j) = \Gamma_0 \exp\left[-\frac{(x_i - x_j)^2}{2\xi_x^2}\right] \exp\left(-\frac{x_i^2 + x_j^2}{4\sigma_x^2}\right). \qquad (8)$$

Since every peak from Γ corresponds to a single pair of coordinates (x_i, x_j), one can map the diffraction intensities of the triangular peak fitting to each coordinate in a (x_i, x_j) two-dimensional space. A one-dimensional cut of this function through $x_i - x_j$ is presented in Fig. 5. The distribution of peaks is symmetric around 0 but only the positive separations are shown in Fig. 5.

The example of the simulation of the NRA diffraction pattern presented in Fig. 4 was performed for a 3 keV beam and an aperture of 400 µm. As can be seen in Fig. 4(*b*), the diffraction pattern was largely oversampled to avoid any loss of information of the mutual coherence function displayed in Fig. 4(*a*). Each peak of the Fourier transform of the diffraction pattern has a scattering form factor of a rectangular slit, $\tilde{T}_{\rm slit}$. They were individually fitted to triangular functions to determine their amplitude at the center coordinate pairs (x_i, x_j), as displayed in Fig. 5(*b*). Finally, a two-dimensional non-linear regression in the space of coordinate pairs (x_i, x_j) and intensities $\Gamma(x_i, x_j)$ was employed to simultaneously fit the coherence length ξ_x and beam size σ_x. Note that the envelope of the Fourier transform of the diffraction pattern does not have a simple exponential decay due to the factor $\exp[(-x_i^2 + x_j^2)/4\sigma_x^2]$. This factor changes non-monotonically for every consecutive (and non-redundant) value of $x_i - x_j$ (see Table 2 for the x_i and x_j values). To effectively display the exponential decay of $\gamma(x_i - x_j)$ the value of the data points $\Gamma(x_i, x_j)$ of the simulation are divided by the factor $\exp[(-x_i^2 + x_j^2)/4\sigma_x^2]$ using the fitted values of σ_x. This results in the data points of Fig. 6 with the best curve fitting of $\Gamma(x_i, x_j) \propto \exp[-(x_i - x_j)^2/2\xi_x^2]$ in the solid red line. In this particular condition of Fig. 6, the best-fitted r.m.s. beam size was 20.3 ± 0.4 µm and the coherence length was 26.2 ± 0.2 µm. The error bars come from the covariance matrix of the two-dimensional non-linear regression of the *SRW* simulation data points.

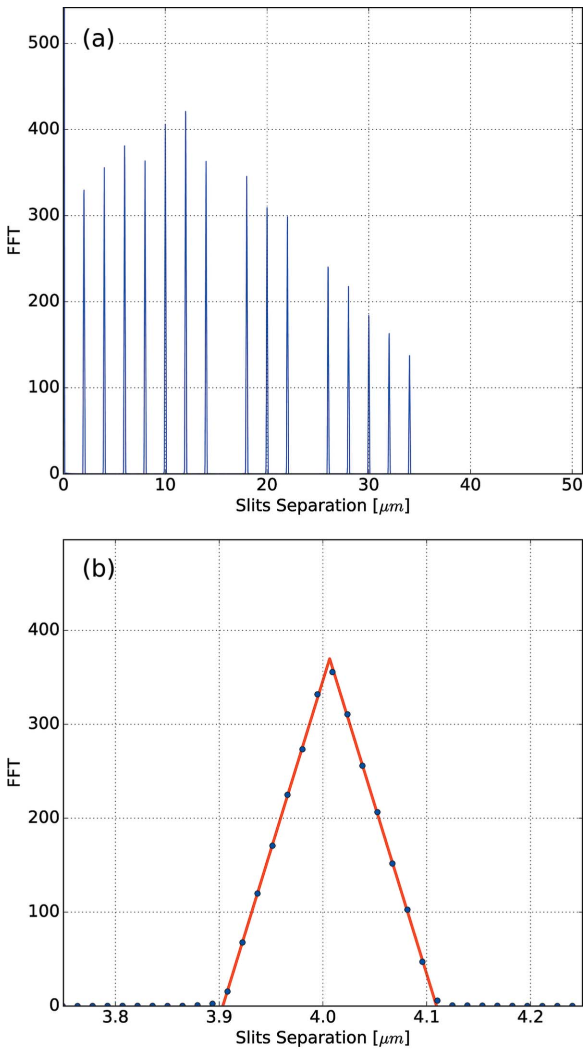

Figure 5
(*a*) Fourier transform of the diffraction pattern fitted by equation (8). (*b*) Zoom of one peak of panel (*a*) showing the triangular function fitting corresponding to the form factor of the slits in the diffraction grating $\tilde{T}_{\rm slit}$.

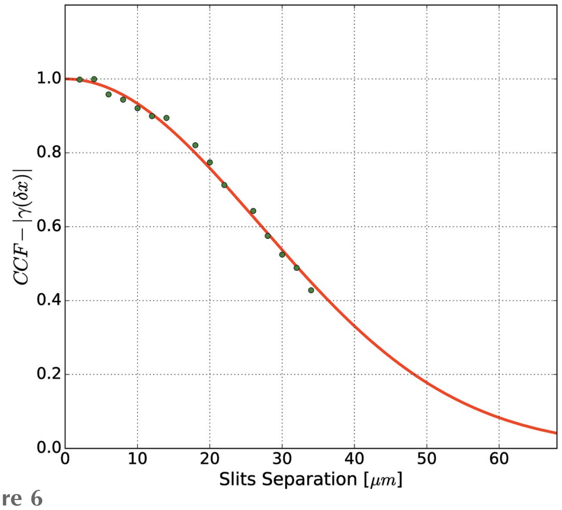

Figure 6
The normalized mutual coherence function $\gamma(x_i - x_j)$. The points are the fitted amplitudes of the peaks in Fig. 5(*b*) and the solid red line is the Gaussian–Schell fit. The fitted r.m.s. beam size was 20.3 ± 0.4 µm and the coherence length was 26.2 ± 0.2 µm.

For some applications (*e.g.* diffraction-enhanced imaging, CDI), partially coherent illumination of samples is acceptable, if more elaborate phase-retrieval schemes are employed as given by Whitehead *et al.* (2009). In this work the conditions that maximize the coherent illumination of the sample are investigated, such that the coherence length is at least twice the r.m.s. beam size. In order to reach this coherent illumination condition, the effective beam emittance is reduced by decreasing its angular acceptance with an aperture before the horizontal focusing mirror. However, as this aperture is reduced, the focus is shifted upstream of the geometric condition. Therefore, before proceeding with the grating diffraction simulations, the focal position for each energy and slit aperture was determined. The focal positions obtained from these simulations in *SRW* for 3 keV and 9 keV (circles) are compared with the Gaussian–Schell model (solid lines) in Fig. 7. Note that for apertures of the order of 600 µm this shift is relatively small, but for smaller apertures the focal position is shifted substantially, by almost 20 m for smaller apertures. These small apertures are, nevertheless, necessary to reach larger coherence lengths.

The apparently counterintuitive effect of the focal position derives purely from undulatory optics and it is expected within the framework of the Gaussian–Schell model. In the thin lens approximation, a fully coherent Gaussian beam source, at a distance p from a thin lens, with a focal length f, is refocused at a distance q, according to the expression from Chu (1966),

$$\frac{q}{f} - 1 = \frac{(p/f) - 1}{[(p/f) - 1]^2 + (Z_{\rm R}/f)^2}, \qquad (9)$$

where $Z_{\rm R}$ is the Rayleigh length of the input beam, which for the partially coherent Gaussian–Schell beam is given by $Z_{\rm R} = \pi\sigma^2/\lambda[1 + (\sigma/\xi)^2]^{-1/2}$ (Gbur & Wolf, 2001). Clearly the distinction from the geometric optics, as obtained through equation (9), is due to an increase of the Rayleigh length that

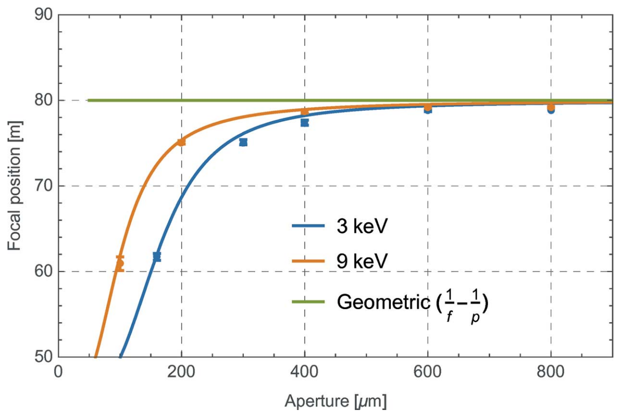

Figure 7
Horizontal focal position (distance from the source to the focal point) as a function of the aperture before the horizontal focusing mirror for 3 keV and 9 keV and the focal position from geometric optics ($1/p + 1/q = 1/f$). The circles correspond to the *SRW* simulation and the full lines correspond to the Gaussian–Schell model with the universal function for the r.m.s. size and divergence. No fitting parameters are used except for the equivalent Gaussian aperture = Aperture/4.55, as given by Singer & Vartanyants (2014).

results from an enhancement in the coherence. In the geometric optics limit, $\xi \rightarrow 0$ and $Z_{\rm R} \rightarrow 0$, reducing equation (9) to the thin lens equation of the geometric optics. In the fully coherent case, $\xi \rightarrow \infty$ and $Z_{\rm R} \rightarrow \pi\sigma^2/\lambda$, leading to the geometric focus of the Gaussian beam (Chu, 1966). As $Z_{\rm R} \gg f$, the focusing condition for a collimated parallel beam is recovered, *i.e.* $q = f$. Obviously, the equation for the focal point in the condition described by Fig. 2 is slightly more complicated due to the combination of propagation, focusing and aperture restriction using the analytical equations presented in Appendix *A*. Nevertheless, expression (9) can be used to understand qualitatively the focusing behavior. Starting from a partially coherent beam and reducing its divergence through apertures, like in Fig. 2, the coherence length is enhanced and, consequently, the Rayleigh length is also increased, bringing the focal position upstream of the geometric focus, as shown in Fig. 7. Surprisingly, the focal length of the achromatic focusing element is affected by the angular acceptance of the aperture in an energy-dependent way (see Fig. 7), *i.e.* for a fixed aperture (small enough to select the coherent part of the beam) the focal positions of different energies occur at different distances. In the example of Fig. 7, for a 200 μm aperture, the focal position for 3 keV and 9 keV differ by more than 5 m. The same effect is expected for any focusing element, like refractive lenses, which are already chromatic. But it is surprising that achromatic elements, like total reflection mirrors, effectively become chromatic in this limit.

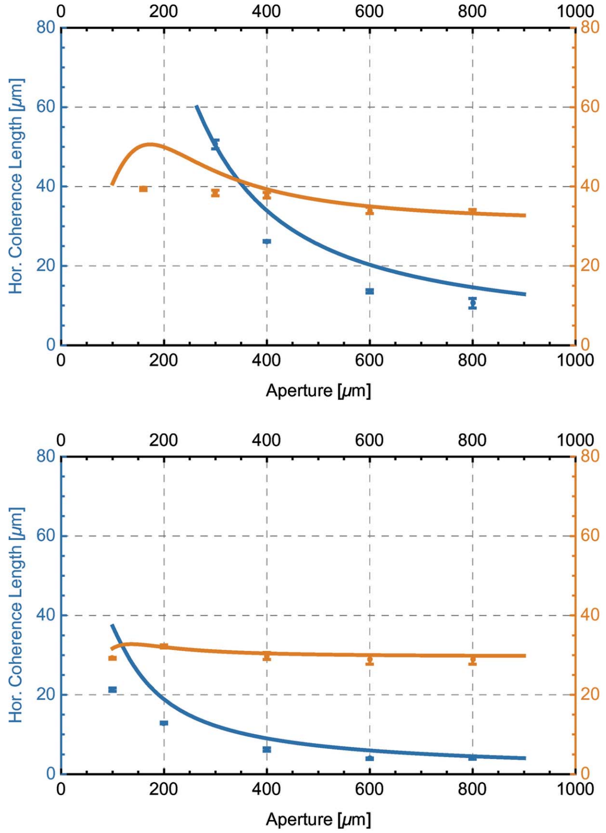

Figure 8
3 keV (upper) and 9 keV (lower) simulations of the coherence length (blue circles) and beam size (orange circles) obtained from the two-dimensional fitting of the NRA diffraction simulation as in Fig. 4 compared with the Gaussian–Schell model (full lines) with the universal function for the r.m.s. size and divergence and with the equivalent Gaussian aperture = Aperture/4.55, as given by Singer & Vartanyants (2014).

For each aperture, a focal position is then defined (see Fig. 7) where the NRA diffraction is simulated. In all simulations, diffraction patterns are observed at 5 m from the NRA. The results for 3 keV and 9 keV for the beam size and coherence length, obtained from the diffraction peak fittings of the *SRW* simulation, are shown as circles in Fig. 8. The Gaussian–Schell model with the universal function for the r.m.s. size and divergence and with the equivalent Gaussian aperture are shown as solid lines in the same figure. To compare the numerical and analytical simulations the r.m.s. aperture is compared with a sharp aperture value divided by 4.55, like the optimal parameter determined by Singer & Vartanyants (2014). No other fitting parameters were used to compare the simulations and the analytical treatment.

To study the effect of mirror imperfections in the wavefront, the simulations presented in Figs. 4 and 5 were repeated, introducing figure errors in the HFM. To model the mirror figure error the meridional height and slope error profiles of Fig. 9 from the DABAM database (Sanchez *et al.*, 2016) were used. Fig. 10 compares the Fourier transform of the diffraction pattern and the resulting normalized correlation function with

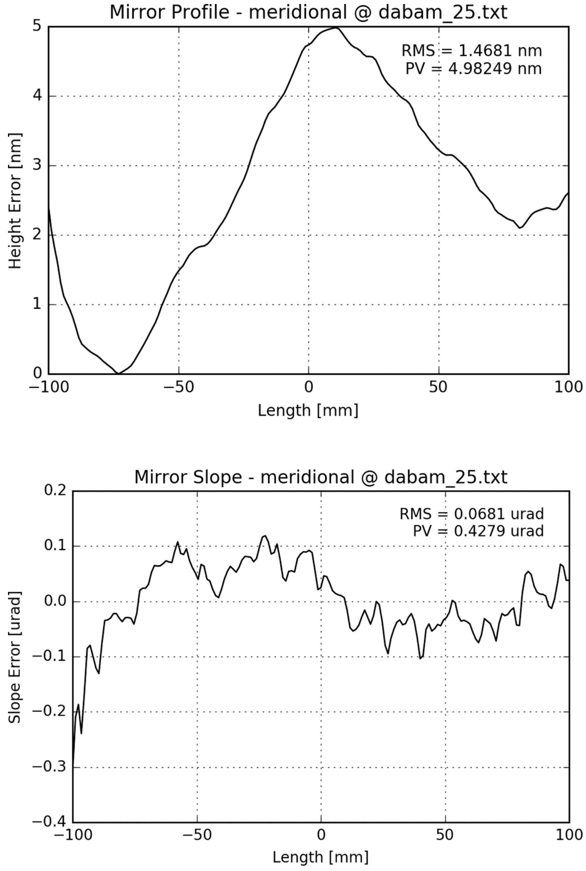

Figure 9
Mirror height and slope profiles used in the wavefront propagation for evaluating the effect of the mirror defects in the coherence length.

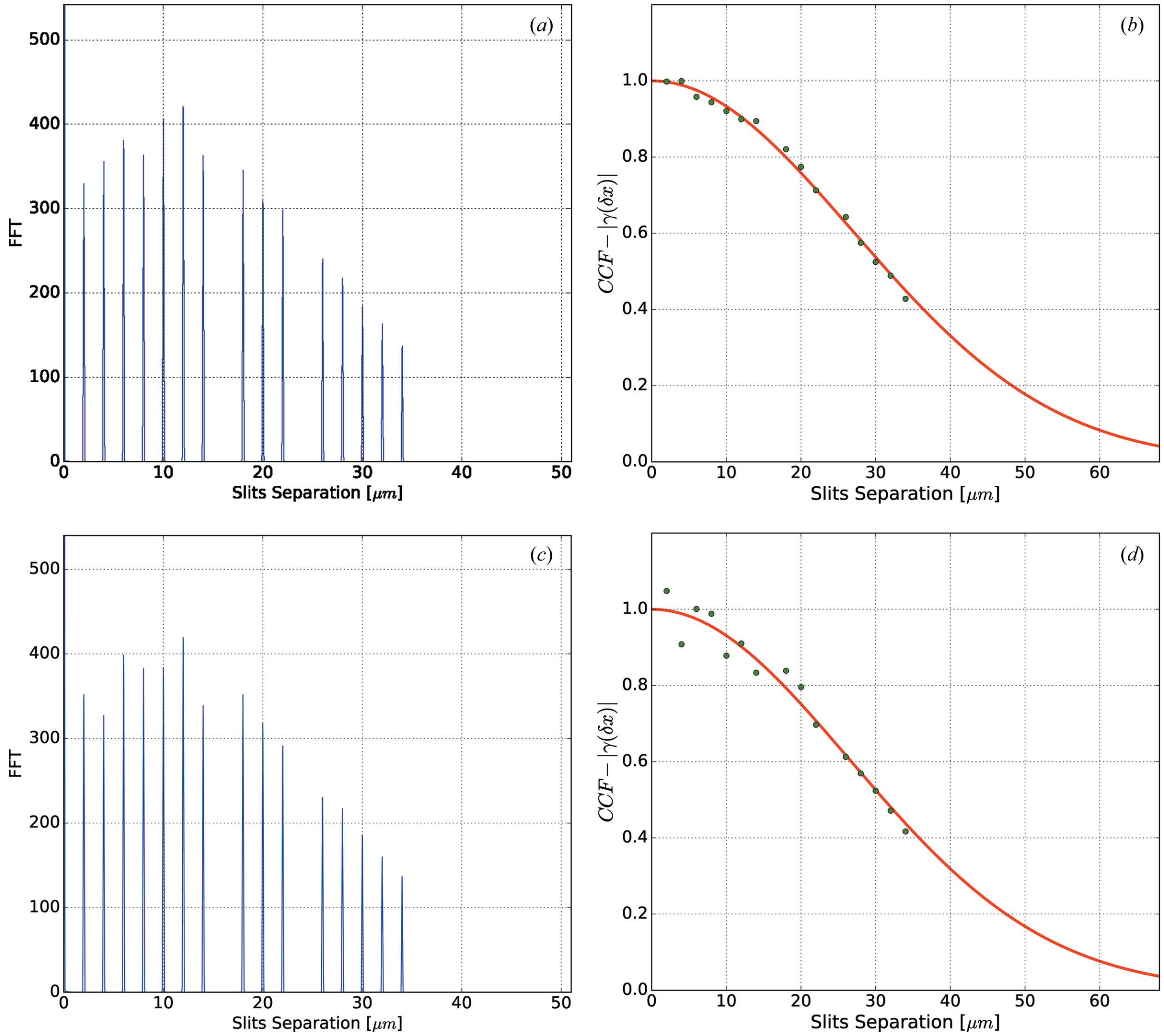

Figure 10

Comparison between the coherence and nano-focusing properties of the partially coherent wave propagation through a perfect mirror (two upper panels) and a mirror with the height and slope profiles of Fig. 9 (lower panels). The upper and lower left panels show Γ while the upper and lower right panels show γ extracted from Γ by using the normalization factor $(I_i)^{1/2}(I_j)^{1/2} = \exp[-(x_i^2 + x_j^2)/4\sigma_x^2]$. The fitting values for the perfect mirror case were σ = 20.3 ± 0.4 µm and ξ = 26.2 ± 0.2 µm, and for the imperfect mirror ξ = 26.1 ± 0.7 µm and σ = 19 ± 1 µm.

and without slope errors. Although the data points are more dispersed in Fig. 10(d), the fittings of the two correlation functions (within error bars) give the same coherence lengths. The apparent dispersion of the data, with values even greater than 1, may look like the simulation has numerical instabilities, but this is not the case. These results were checked by varying the number of macro-electrons and the precision parameters, reaching the same results. In fact, the dispersion is caused by random deviations from the Gaussian wavefront. The normalization factor $(I_i)^{1/2}(I_j)^{1/2}$ applied to Γ to obtain γ is considered as a Gaussian irradiance, *i.e.* $(I_i)^{1/2}(I_j)^{1/2} = \exp[-(x_i^2 + x_j^2)/4\sigma_x^2]$. However, this normalization is non-homogeneous, since the irradiance at the sample position is distorted by the mirror figure errors. Despite this dispersion of the normalized data, the coherence length extracted from the two-dimensional fitting was 26.1 ± 0.7 µm (which is equivalent to the perfect mirror case of 26.2 ± 0.2 µm) and the r.m.s. beam size was 19 ± 1 µm (which is also equivalent to the perfect mirror case of 20.3 ± 0.4 µm). Therefore, as expected, the mirror imperfections distort the wavefront, as shown by the tails in the beam shape at the focal point, but practically do not affect the coherence length for this level of imperfection.

6. Summary

Designing beamlines for optimally extracting the coherent flux available in third- and fourth-generation storage rings goes beyond the traditional ray-tracing approach and needs to take into account the wave nature of the radiation propagating through the optical elements. Even though fourth-generation machines have a high coherent flux fraction, the use of apertures to effectively reduce the X-ray radiation emittance is almost always necessary. Here the coherence length and coherent fraction of a slightly focused X-ray beam from an undulator in a fourth-generation storage ring was calculated by simulating the wavefront propagation through a non-redundant array of slits. This approach reduced the computational time for simulating a coherent beamline by a factor of the order of 10, since instead of simulating the propagation through double slits (as typically done for evaluating the mutual coherence function) the entire coherence degree is obtained in a single simulation. It was shown how the coherence length at the focal point can be controlled by an aperture before the focusing element and that, in order to reach coherence lengths of the order of twice the r.m.s. beam size, it is necessary to use apertures of the order of 300 µm at 3 keV and 100 µm at 9 keV. Unless the focal length of the focusing element is changed, this energy change places the focus at these two energies at about 15 m apart from each other. Therefore, in coherent applications, in combination with coherent selection apertures, even total reflection mirrors can become effectively chromatic elements. These numerical results were shown to be in qualitative agreement with the analytical propagation of the Gaussian–Schell model using the r.m.s. size and divergence from the universal functions for undulator radiation sources. The analytical propagation of the Gaussian–Schell model can be used to estimate the beam properties before carrying out the full wavefront propagation. Together with the method of using the NRA for simulating the coherent properties of the beam, this allows a more efficient design of beamlines for coherent applications.

APPENDIX *A*

The *ABCD* formalism for the Gaussian–Schell model

The propagation of a Gaussian–Schell beam through a series of optical elements forming a beamline can be represented by a transfer matrix of the form

$$\begin{pmatrix} A & B \\ C & D \end{pmatrix}.$$

The complex elements of the transfer matrix, A, B, C and D, are obtained through the multiplication of the transfer matrices of the individual optical elements as for a conventional Gaussian beam propagation.

The major difference from the pure Gaussian case is that, at the output of the optical system, the Gaussian–Schell beam parameters, radius of curvature ($R_{\rm o}$), r.m.s. size ($\sigma_{\rm o}$) and coherence length ($\xi_{\rm o}$) are obtained from the incoming beam parameters ($R_{\rm i}$, $\sigma_{\rm i}$ and $\xi_{\rm i}$, respectively) through the equations adapted from Dragoman (1995),

$$\begin{aligned}\frac{\Delta}{R_{\rm o}} &= C\cdot A + \frac{A\cdot D + C\cdot B}{R_{\rm i}} + D\cdot B\left(\frac{1}{R_{\rm i}^2} + \frac{1}{k^2\xi^2\sigma^2} + \frac{1}{4k^2\sigma^4}\right) \\ &\quad - \left(\frac{1}{\xi_{\rm i}^2} + \frac{1}{2\sigma_{\rm i}^2}\right)\frac{(A\times D + C\times B)}{k},\end{aligned}$$

$$\begin{aligned}-\frac{\Delta}{\sigma_{\rm o}^2} &= \frac{2k}{R_{\rm i}^2}(C\times B - A\times D) + \left(\frac{2}{\xi_{\rm i}^2} + \frac{1}{\sigma_{\rm i}^2}\right)(C\cdot B - A\cdot D) \\ &\quad + 2kC\times A + 2kD\times B\left(\frac{1}{R_{\rm i}^2} + \frac{1}{k^2\xi^2\sigma^2} + \frac{1}{4k^2\sigma^4}\right) + \frac{2}{\xi_{\rm i}^2},\end{aligned}$$

$$\frac{\Delta}{\xi_{\rm o}^2} = \frac{1}{\xi_{\rm i}^2}$$

where

$$\Delta = \left| A + B\left[\frac{1}{R_{\rm i}} + \frac{i}{k}\left(\frac{1}{\xi_{\rm i}^2} + \frac{1}{2\sigma_{\rm i}^2}\right)\right]\right|^2 - \frac{|B|^2}{k^2\xi_{\rm i}^4}.$$

The same notation of Dragoman (1995) was adopted, where

$$U\cdot V = \Re(U)\,\Re(V) + \Im(U)\,\Im(V)$$

and

$$U\times V = \Re(U)\,\Im(V) - \Re(U)\,\Im(V).$$

The complex numbers U and V can be any of the complex numbers A, B, C and D of the optical system transfer matrix, which are considered to have a unit determinant.

Acknowledgements

We thank Ruben Reiningen for encouraging us to look for these coherence effects through wavefront propagation. We thank José Roque, Hélio Tolentino, Liu Lin, Ricardo Rodrigues and Ian McNulty for numerous stimulating discussions. We thank Oleg Chubar for help with several aspects of *SRW*. We also acknowledge the use of the computing cluster from LNCC – Laboratório Nacional de Computação Científica.

References

Bazarov, I. V. (2012). *Phys. Rev. ST Accel. Beams*, **15**, 050703.

Chu, T. S. (1966). *Bell Syst. Tech. J.* **45**, 287–299.

Chubar, O., Berman, L., Chu, Y. S., Fluerasu, A., Hulbert, S., Idir, M., Kaznatcheev, K., Shapiro, D., Shen, Q. & Baltser, J. (2011). *Proc. SPIE*, **8141**, 814107.

Chubar, O., Fluerasu, A., Berman, L., Kaznatcheev, K. & Wiegart, L. (2013). *J. Phys. Conf. Ser.* **425**, 162001.

Dragoman, D. (1995). *Appl. Opt.* **34**, 3352–3357.

Friberg, A. T. & Turunen, J. (1988). *J. Opt. Soc. Am. A*, **5**, 713–720.

Gbur, G. & Wolf, E. (2001). *J. Mod. Opt.* **48**, 1735–1741.

Geloni, G., Saldin, E., Schneidmiller, E. & Yurkov, M. (2008). *Nucl. Instrum. Methods Phys. Res. A*, **588**, 463–493.

Kauderer, M. (1991). *Appl. Opt.* **30**, 1025–1035.

Kim, K.-J. (1985). *Proc. SPIE*, **0582**, 2.

Lindberg, R. R. & Kim, K.-J. (2015). *Phys. Rev. ST Accel. Beams*, **18**, 090702.

Liu, L., Milas, N., Mukai, A., Resende, X. & Sá, F. (2014). *J. Synchrotron Rad.* **21**, 904–911.

Mandel, L. & Wolf, E. (1965). *Rev. Mod. Phys.* **37**, 231–287.

Miao, J., Ishikawa, T., Robinson, I. K. & Murnane, M. M. (2015). *Science*, **348**, 525–530.

Sanchez del Rio, M., Bianchi, D., Cocco, D., Glass, M., Idir, M., Metz, J., Raimondi, L., Rebuffi, L., Reininger, R., Shi, X., Siewert, F., Spielmann-Jaeggi, S., Takacs, P., Tomasset, M., Tonnessen, T., Vivo, A. & Yashchuk, V. (2016). *J. Synchrotron Rad.* **23**, 665–678.

Schroer, C. G. & Falkenberg, G. (2014). *J. Synchrotron Rad.* **21**, 996–1005.

Singer, A. & Vartanyants, I. A. (2014). *J. Synchrotron Rad.* **21**, 5–15.

Skopintsev, P., Singer, A., Bach, J., Müller, L., Beyersdorff, B., Schleitzer, S., Gorobtsov, O., Shabalin, A., Kurta, R. P., Dzhigaev, D., Yefanov, O. M., Glaser, L., Sakdinawat, A., Grübel, G., Frömter, R., Oepen, H. P., Viefhaus, J. & Vartanyants, I. A. (2014). *J. Synchrotron Rad.* **21**, 722–728.

Tanaka, T. (2014). *Phys. Rev. ST Accel. Beams*, **17**, 060702.

Tanaka, T. & Kitamura, H. (2009). *J. Synchrotron Rad.* **16**, 380–386.

Vartanyants, I. A. & Singer, A. (2010). *New J. Phys.* **12**, 035004.

Veen, F. van der & Pfeiffer, F. (2004). *J. Phys. Condens. Matter*, **16**, 5003–5030.

Whitehead, L. W., Williams, G. J., Quiney, H. M., Vine, D. J., Dilanian, R., Flewett, S., Nugent, K. & McNulty, I. (2009). *Phys. Rev. Lett.* **103**, 243902.